

Unveiling an Hourglass-Shaped Magnetic Field toward IRDC G351.77–0.53

O. R. Jadhav^{1,2*}, L. K. Dewangan¹, I. I. Zinchenko³, Thushara G. S. Pillai⁴,
Patricio Sanhueza⁵, A. K. Maity¹, Ram K. Yadav⁶, and Saurabh Sharma⁷

¹Physical Research Laboratory, Navrangpura, Ahmedabad - 380 009, India.

²Indian Institute of Technology Gandhinagar Palaj, Gandhinagar 382355, India.

³Institute of Applied Physics of the Russian Academy of Sciences, 46 Ulyanov st., Nizhny Novgorod 603950, Russia.

⁴Haystack Observatory, Massachusetts Institute of Technology, 99 Millstone Road, Westford, MA 01886, USA.

⁵Department of Astronomy, School of Science, The University of Tokyo, 7-3-1 Hongo, Bunkyo, Tokyo 113-0033, Japan.

⁶National Astronomical Research Institute of Thailand (Public Organization), 260 Moo 4, T. Donkaew, A. Maerim, Chiangmai 50180, Thailand.

⁷Aryabhata Research Institute of Observational Sciences, Manora Peak, Nainital 263002, India.

ABSTRACT

We present the SOFIA/HAWC+ 214 μm polarimetric observations toward the infrared dark cloud G351.77-0.53 (hereafter G351), complemented by existing multi-wavelength data sets. Infrared excess from the embedded sources indicate ongoing star formation activity in the cloud. The G351 cloud hosts two prominent star-forming clumps, i.e., c1 and c2. The plane-of-the-sky magnetic field lines from *Planck* observations are predominantly oriented perpendicular to the filament’s major axis. Magnetic field orientations from SOFIA/HAWC+ 214 μm observations reveal distinct hourglass-shaped field configuration toward c1, while the field lines remain perpendicular to the rest of the filament. Using the Davis-Chandrasekhar-Fermi method, we estimate a mean plane-of-the-sky magnetic field strength of $\sim 147 \pm 60$ μG in the G351 filament, with values reaching ~ 0.8 mG toward c1. The mass-to-flux ratio analysis indicates that the filament is magnetically transcritical, where the gravitational and magnetic field energies are comparable. The hourglass-shaped magnetic field observed toward c1 could result from magnetically regulated gravitational collapse, the alignment of converging sub-filaments with the magnetic field, or a combination of both processes. The energy budget analysis further indicates that magnetic fields play an important role in governing the cloud’s gas dynamics, followed by contributions from turbulence and gravity.

Key words: stars: massive – ISM: magnetic fields – galaxies: star formation – dust, extinction

1 INTRODUCTION

Filaments are prevalent structures within the interstellar medium (ISM) and are linked to both low- and high-mass star formation activities (Arzoumanian et al. 2011; André et al. 2014). These filamentary structures harbor dense cores that eventually form stars. Clouds or filamentary structures that are particularly dense and cold, and appear in absorption against the bright mid-infrared (MIR) Galactic background, are referred to as infrared (IR) dark clouds (IRDCs). Owing to their high column densities ($N(\text{H}_2)$) and low temperatures, IRDCs are considered to trace the earliest stages of star formation (Rathborne et al. 2006; Chambers et al. 2009; Sanhueza et al. 2012). These IRDCs harbor dense cores that eventually give rise to massive stars and stellar clusters. The intense radiative and

mechanical feedback from these massive stars disrupts the initial conditions that led to their formation.

Several observational studies have revealed ordered magnetic field (B-field) morphologies toward these filamentary structures (Planck Collaboration et al. 2016; Stephens et al. 2025; Coudé et al. 2025), indicating that B-fields play a dynamically significant role in regulating the physical processes involved in star formation. The B-field morphology is generally perpendicular to high- $N(\text{H}_2)$ ($> 5 \times 10^{21} \text{ cm}^{-2}$) (Soler & Hennebelle 2017) filaments, whereas in low- $N(\text{H}_2)$ ($< 5 \times 10^{21} \text{ cm}^{-2}$) filaments, the field orientations can be parallel or more randomly distributed. These trends are observed in several magnetohydrodynamical (MHD) simulations as well (Nakamura & Li 2008; Soler et al. 2013; Seifried & Walch 2015; Chen & Ostriker 2015; Maity et al. 2024). However, the exact role of B-fields and their interplay with gravity and turbulence, especially in IRDCs still remains poorly understood. In the literature, the detailed

* E-mail: omkar@prl.res.in

study of B-field structure has been carried out toward only a handful of IRDCs, such as G11.11-0.12 (Chen et al. 2023; Ngoc et al. 2023; Truong et al. 2025), G14.225-0.506 (Santos et al. 2016; Añez-López et al. 2020), G28.34+0.06 (Law et al. 2024; Liu et al. 2024; Hwang et al. 2025), G34.43+0.24 (Tang et al. 2019; Soam et al. 2019; Pravash et al. 2025), G47.06+0.26 (Stephens et al. 2022; Jadhav et al. 2025), and G11.92 (Sanhueza et al. 2025). B-fields are thought to influence star formation processes within IRDCs by potentially reducing small-scale fragmentation, aiding the formation of massive stars, and guiding gas flows along preferred directions; however, the observational evidence remain limited (Pillai et al. 2015). Therefore, studying the B-field structure in filamentary IRDCs is essential for understanding its role and interplay with turbulence and gravity.

G351.77-0.53 (G351 hereafter) is a well-studied massive star-forming region hosting massive protocluster IRAS 17233-3606 at its center (Simon et al. 2006; Leurini et al. 2008; Zapata et al. 2008; Leurini et al. 2011b; Ryabukhina & Zinchenko 2021; Beuther et al. 2025; Ishihara et al. 2024; Ginsburg et al. 2023, and references within). The region hosts 6.7 GHz Class II CH₃OH masers (Norris et al. 1993; Walsh et al. 1998; Beuther et al. 2017, 2019) and several outflow activities (Leurini et al. 2009, 2011a, 2013; Klaassen et al. 2015; Sandoval-Garrido et al. 2025). Leurini et al. (2019) investigated the G351 cloud with Atacama Pathfinder Experiment (APEX) and *Herschel* observations and revealed that the cloud consists of a main filamentary structure surrounded by a network of filaments. The gas kinematics studies shows that the filament has a coherent velocity of ~ 3 km s⁻¹ (Leurini et al. 2011b, 2019). The distance to this source has been highly debated, with the values ranging from 0.7 to 2.2 kpc being used in previous studies (Leurini et al. 2011b; Ryabukhina & Zinchenko 2021; Motte et al. 2022). However, a recent study of the G351 cloud by Reyes-Reyes et al. (2024), based on Gaia DR3 data, estimated a distance of ~ 2.0 kpc based on the average parallax of the likely members of the cloud. We adopt this distance for our current work.

Despite these extensive studies, the structure of the B-field and its influence on massive star formation activity within the G351 cloud remain unexplored. Therefore, a comprehensive investigation using polarimetric observations is essential for characterizing the B-field morphology in this region. Moreover, the relative contributions of magnetic, gravitational, and kinetic energies is crucial to assess whether the B-fields govern the cloud's dynamics or if gravity and turbulence play a more dominant role. In this context, our current study focuses on investigating the role of B-fields using the far-infrared (FIR) polarimetric data to estimate the B-field morphology, strength, and energy. Additionally, this study incorporates complementary multi-wavelength datasets spanning from radio to IR wavelengths.

This paper is organized as follows. In Section 2, we describe the data selection. In Section 3, we present the outcomes of our multi-wavelength data analysis. In Section 4, we discuss the implications of our results. Finally, the findings are summarized and the conclusions are presented in Section 5.

2 DATASETS USED

In this work, we analyzed multi-wavelength data sets toward the G351 cloud, primarily in the area of $0.22^\circ \times 0.27^\circ$ centered at Right Ascension (RA) = 17h26m33s and Declination (Dec) = -36d08m03s. A summary of all the data sets analyzed in this study is presented below.

2.1 NIR and MIR data

We acquired Near-Infrared (NIR) and MIR images at 3.6–8.0 μm (resolution $\sim 2''$; plate scale $\sim 0''.6$) from the *Spitzer* Galactic Legacy Infrared Mid-Plane Survey Extraordinaire (GLIMPSE; Benjamin et al. 2003) survey. The MIR 12.0 μm image was obtained from the Unblurred Coadds of the Wide-field Infrared Survey Explorer (WISE) Imaging (unWISE) survey (resolution $\sim 6''$; Lang 2014), which provides WISE images with an improved signal-to-noise ratio.

2.2 FIR data

The G351 cloud was observed with the Stratospheric Observatory for Infrared Astronomy (SOFIA) telescope using the High-resolution Airborne Wideband Camera Plus (HAWC+) instrument (Harper et al. 2018) at 214 μm (or Band E). These observations were taken as part of a survey program (PI: Thushara Pillai; Proposal ID: 07_0238). We used the Level 4 data products in this study which have a spatial resolution of $\sim 18''.2$ and a pixel scale of $\sim 4''.55$.

2.3 Sub-millimeter data

The 870 μm emission data (resolution $\sim 18''.2$) were taken from the Atacama Pathfinder Experiment (APEX) Telescope Large Area Survey of the GALaxy (ATLASGAL; Schuller, F. et al. 2009). The catalog presented by Urquhart et al. (2017) provides details for roughly 8,000 dense clumps in the Galactic disc based on the ATLASGAL data. They also provided the velocities, distances, luminosities, and masses of clumps (see Urquhart et al. 2017, for more details). Using this catalog, we identified the positions of dense clumps associated with the G351 cloud. To infer the POS B-field orientation toward the cloud at larger scales (~ 10 pc) we utilized the 353 GHz polarization maps obtained from the Planck Legacy archive observed as part of the Planck mission. The data provides the I , Q , and U polarization maps observed using the High Frequency Instrument (HFI) (Lamarre et al. 2010) on the Planck satellite, with a spatial resolution of $5'$ (Planck Collaboration et al. 2015).

2.4 Millimeter data

The C¹⁸O(2–1) molecular line data used in this study are the same as those analyzed by Ryabukhina & Zinchenko (2021), obtained from observations conducted with the APEX radio telescope between 2010 and 2017 (projects O-085.F-9323, O-086.F-9316, O-097.F-9303, O-098.F-9306) using SHeFI receivers. The resolution of the data is $\sim 32''$. The data are converted to the main beam temperature scale using the main beam efficiencies (η_{mb}) presented on the APEX web site. The antenna temperature is converted into main beam temperature using the formula $T_{\text{mb}} = T_{\text{A}}/\eta_{\text{mb}}$, where $\eta_{\text{mb}} = 0.75$. Further details of the APEX C¹⁸O(2–1) observations and data processing can be found in Ryabukhina & Zinchenko (2021).

2.5 Radio data

We have used the South African Radio Astronomy Observatory (SARAO) MeerKAT Galactic Plane Survey (SMGPS) 1.3 GHz continuum emission data (resolution $\sim 8''$; sensitivity $\sim 22 \mu\text{Jy beam}^{-1}$; Goedhart et al. 2024).

3 RESULTS

3.1 Physical environment toward the G351 IRDC

Figure 1a presents the unWISE 12.0 μm image of the G351 cloud, overlaid with diamonds marking the positions of the ATLASGAL clumps. The image reveals the filamentary structure of G351 seen in absorption against the MIR background. Most of the ATLASGAL clumps are distributed toward the northern region of the filament. We also identified Class I young stellar objects (YSOs) toward the cloud using the [4.5]–[5.8] versus [3.6]–[4.5] color–color diagram (CCD) (Hartmann et al. 2005; Getman et al. 2007). Although these plots are not shown in this paper, further details can be found in Dewangan et al. (2015). A total of 53 Class I YSOs are identified using this method, and their locations are marked with red circles in Figure 1a. Most of these Class I YSOs are seen toward the filament, confirming ongoing star formation activity within the filamentary cloud. Figure 1b shows the ATLASGAL 870 μm contours overlaid with SMGPS 1.3 GHz continuum emission contours, revealing substructures within the cloud. The SMGPS 1.3 GHz continuum emission is concentrated only toward two clumps (c1 and c2), while the rest of the cloud shows little to no radio emission. The absence of radio emission toward most of the filament indicates that the filament is in an early stage of star formation. To further explore the star formation activity, we generated *Spitzer* 4.5 μm /3.6 μm ratio map. Figure 1d displays the resulting ratio map, showing several bright areas (see arrows in Figure 1d). These bright areas are dominated by the 4.5 μm emission and are consistent with the locations of the dust clumps. This excess 4.5 μm emission could be due to the ionized emission at 4.05 μm or the H_2 emission at 4.69 μm . Given the presence of Class I protostars towards these bright areas, the emissions likely correspond to H_2 features, while the darker areas trace polycyclic aromatic hydrocarbon (3.3 μm PAH emission in *Spitzer* 3.6 μm band), indicating the presence of warm dust.

3.2 POS B-field orientations from the SOFIA/HAWC+ and Planck

To infer the POS B-field morphology toward the G351 cloud, we employ the SOFIA/HAWC+ 214 μm polarization data (resolution $\sim 18''$). The Q , and U Stokes maps are used to obtain the polarization angle. The polarization angle is estimated using

$$\theta = \frac{1}{2} \arctan 2(U, Q) \quad (1)$$

The B-field position angles are obtained by rotating the polarization vectors by 90° . We retained the vectors which satisfy the following criteria: $p/\sigma_p > 3$, $I/\sigma_I > 100$, and $p < 30$ (Zielinski & Wolf 2022; Li et al. 2022; Tram et al. 2023; Lietzow-Sinjen et al. 2025). Figure 2a shows the overlay of the segments showing the SOFIA/HAWC+ 214 μm B-field orientations on the corresponding intensity map of the G351 cloud. The B-field lines exhibit an hour-glass morphology toward the central massive clump (c1), whereas in the rest of the cloud (including c2), the field orientations are predominantly perpendicular to the major axis of the filament. This behavior is also more clearly illustrated in the Line Integral Convolution (LIC) map of the B-fields presented in Figure 2b. The LIC map is generated using the *magnetar* package (Soler et al. 2013). In Figure 2b, the red and blue arrows indicate the direction of the outflow, while the black dashed line shows the direction of the velocity gradient reported by Klaassen et al. (2015). Since the study by Klaassen et al. (2015) was conducted at core scales (~ 0.01

pc), a direct and detailed comparison with the B-field morphology traced by the SOFIA/HAWC+ observations in this study is not feasible, and require high-resolution polarimetric observations. Figure 2c shows the segments indicating the B-field orientations from SOFIA/HAWC+ 214 μm data, with their lengths corresponding to the degree of polarization. We also inferred the POS B-field direction using the Planck 353 GHz polarization data (see Figure 2d). The B-field vectors inferred from the Planck data are predominantly perpendicular to the G351 cloud.

3.3 Molecular gas kinematics

To study the gas kinematics toward the G351 cloud, we utilized the $\text{C}^{18}\text{O}(2-1)$ molecular line observations from APEX telescope.

3.3.1 Moment maps and PV diagram

Figure 3a shows the $\text{C}^{18}\text{O}(2-1)$ integrated intensity (moment-0) map toward the G351 cloud between $[-5, 10]$ km s^{-1} . The moment-0 map retains the filamentary structure of the cloud, with high intensity toward c1. The intensity-weighted mean velocity (moment-1) map is shown in Figure 3b, which allows us to examine the velocity distribution within the cloud. The map indicates that the entire filament exhibits a coherent velocity of approximately -3 km s^{-1} . The moment-2 map (see Figure 3c) allows us to study the velocity dispersion toward the cloud. The moment-2 map shows high velocity dispersion (up to ~ 2 km s^{-1}) toward the c1. To further understand the gas kinematics toward the G351 cloud, we generated the $\text{C}^{18}\text{O}(2-1)$ position-velocity (PV) diagram along the spine of the filament (see Figure 4).

3.3.2 Mass estimation using $\text{C}^{18}\text{O}(2-1)$

We have calculated the gas mass of the G351 cloud using the $\text{C}^{18}\text{O}(2-1)$ emission. Assuming the system in local thermodynamic equilibrium (LTE), we can calculate the column density of a linear molecule using the equation (Mangum & Shirley 2015)

$$N = \frac{3h}{8\pi^3 \mu^2 S} \frac{Q_{\text{rot}}}{g_J g_I g_K} \frac{\exp\left(\frac{E_{\text{up}}}{kT_{\text{ex}}}\right)}{\exp\left(\frac{h\nu}{kT_{\text{ex}}}\right) - 1} \times \frac{1}{J(T_{\text{ex}}) - J(T_{\text{bg}})} \int T_{\text{r}} dv, \quad (2)$$

where the integral is performed over velocity range $[-5, 10]$ km s^{-1} . Here $J(T) = \frac{h\nu/k}{\exp(h\nu/kT) - 1}$ and $T_{\text{bg}} = 2.73$ K is the cosmic microwave background temperature. The excitation temperature (T_{ex}) for the target source is assumed to be 20 K (mean T_{d} of ATLASGAL clumps toward the filament). The symbol μ stands for the dipole moment of the molecule. The degeneracy (g_J) is $2J_u + 1 = 5$, g_I is nuclear spin degeneracy, and g_K is K degeneracy, both are equal to 1 (for C^{18}O). The line strength (S) is $\frac{J_u}{2J_u + 1} = \frac{2}{5}$, where J_u is the rotational quantum number of the upper state (i.e., $J_u = 2$ for the $J = 2 - 1$ transition). E_{up} is the energy of the upper state. We have adopted an approximated formula for the rotational partition function (Q_{rot}) mentioned in various previous studies (e.g., Mangum & Shirley 2015; Yuan et al. 2016), $Q_{\text{rot}} = \frac{kT}{hB} + \frac{1}{3}$, where B is the rotational constant of the molecule. Other molecular parameters have been adopted from the Jet Propulsion Laboratory (JPL) Molecular Spectroscopy database and spectral line catalog (Pickett et al. 1998).

Using the integrated $\text{C}^{18}\text{O}(2-1)$ emission at $[-10, 5]$ km s^{-1}

in Equation 2, the C¹⁸O column density map is produced. Now considering the column density ratio between H₂ and C¹⁸O (i.e., $\frac{N(\text{H}_2)}{N(\text{C}^{18}\text{O})} = 4.8 \times 10^6$ at a Galactocentric distance of 6.4 kpc; Liu et al. 2013), we have obtained the $N(\text{H}_2)$ map. The resultant column density map is shown in Figure 3d. We estimate the mass of the cloud using

$$M = \mu_{\text{H}_2} m_{\text{H}} a_{\text{pixel}} \Sigma N(\text{H}_2), \quad (3)$$

where μ_{H_2} is the H₂ mean molecular weight (assumed to be 2.8), m_{H} is the mass of the hydrogen atom, a_{pixel} is the physical area subtended by 1 pixel in cm², and $\Sigma N(\text{H}_2)$ is the integrated column density above contour level of 1.6×10^{22} cm⁻² (see Figure 3d). The total mass of the molecular cloud is $\sim 4150 M_{\odot}$. The uncertainty in the derived mass is dominated by the adopted gas-to-dust ratio and the assumption of LTE, contributing at least a 50% uncertainty. However, the actual uncertainty may be significantly higher. This estimated mass is roughly half of the previous estimate for this filament (Ryabukhina & Zinchenko 2021), when scaled to the same distance. The difference arises because the previous study used a dust temperature map as T_{ex} to derive the $N(\text{H}_2)$ at each pixel, whereas in this work we adopt a constant T_{ex} value. This is due to the saturation of the *Herschel* 160, 250, and 350 μm bands toward the central clump c1. In addition, previous studies adopted a slightly larger integration area and a different C¹⁸O–H₂ conversion factor, which together result in a lower total mass estimate in our study.

3.4 Estimation of magnetic field strength

We employ the SOFIA/HAWC+ 214 μm polarization observations to estimate the POS B-field strength (B_{POS}) toward the G351 cloud. The B_{POS} value is estimated using the Davis-Chandrasekhar-Fermi (DCF) method (Chandrasekhar & Fermi 1953). However, we use a variant of the DCF method by Crutcher (2012) to estimate the B_{POS} using,

$$B_{\text{POS}} = Q \sqrt{4\pi\rho} \frac{\sigma_{\text{VNT}}}{\delta_{\theta}} \approx 9.3 \sqrt{n(\text{H}_2)} \frac{\Delta V_{\text{nt}}}{\delta_{\theta}} (\mu\text{G}), \quad (4)$$

where Q is the correction factor taken as 0.5, ρ is the gas density in g cm⁻³, σ_{VNT} is the non-thermal velocity dispersion in km s⁻¹, δ_{θ} is the polarization angle dispersion in degrees, $n(\text{H}_2)$ is the volume density in cm⁻³, and ΔV_{nt} is the FWHM of the non-thermal velocity component in km s⁻¹. In the following subsections, we derive these parameters for the G351 cloud regions to estimate B_{POS} values.

3.4.1 Volume density

Using the $N(\text{H}_2)$ map and mass derived in Section 3.3.2, the volume density ($n(\text{H}_2)$) of the filament can be obtained using the following equation

$$n(\text{H}_2) = \frac{ML}{\pi R^2}, \quad (5)$$

where M is the mass of the filament, L is the length of the filament, and R is the radius of the filament. The length of the filament is calculated using the RadFil¹ algorithm (Zucker & Chen 2018) on the $n(\text{H}_2)$ map obtained in Section 3.3.2. This analysis yields a filament length of approximately 7.8 pc. The RadFil package allows to fit the $n(\text{H}_2)$ profile along the spine of the filament with a Plummer-like Function (André et al. 2014). The radius of the

filament is adopted to be equal to its flattening radius, as derived from the fitted profile i.e., ~ 0.55 pc. To generate the volume density map of the G351 cloud, we adopt the relation $n(\text{H}_2) = N(\text{H}_2)/W$, where W is the width of the filament. The width of the filament is taken as $2 \times R_{\text{flat}}$ (André et al. 2014).

3.4.2 Polarization angle dispersion

We use the structure function method to estimate the polarization angle dispersion toward G351 (Hildebrand et al. 2009; Houde et al. 2009). According to this method, the B_{POS} can be estimated using Eq. 4 but the polarization angle dispersion $\delta\theta$ is replaced by the structure function of the polarization angles, so-called angular structure function. The angular structure function, $D_{\theta}^{1/2}$, at an angular scale ℓ is estimated as (Hildebrand et al. 2009):

$$D_{\theta}^{1/2}(\ell) \equiv \langle \Delta\theta^2(\ell) \rangle^{1/2} = \left\{ \frac{1}{N(\ell)} \sum_{i=1}^{N(\ell)} [\theta(x) - \theta(x + \ell)]^2 \right\}^{1/2}, \quad (6)$$

where $\langle \dots \rangle$ denotes an average, $\Delta\theta(\ell) \equiv \theta(x) - \theta(x + \ell)$ is the polarization angle difference between individual pairs of polarization vectors at position x and $x + \ell$, where $\theta(x)$ and $\theta(x + \ell)$ are the corresponding polarization angles at position x and $x + \ell$, respectively, and $N(\ell)$ is number of pairs of vectors with a displacement of ℓ . At scales ℓ much smaller than the scale for a variation of the large-scale B-field structure (typically of $\sim 5'$, as seen by the *Planck* observations), the total angular dispersion function can be expressed as (Schleuning 1998; Houde et al. 2004; Hildebrand et al. 2009):

$$D_{\theta}(\ell) \simeq b^2 + m^2\ell^2 + \sigma_{\text{M}}^2(\ell), \quad (7)$$

where b represents the turbulent component of B-fields (B_{t}), $m\ell$ describes the large-scale structure of B-fields (B), and $\sigma_{\text{M}}(\ell)$ is subject to measurement uncertainties. Also, the ratio between the turbulent and large-scale B-field strength indicates the angular dispersion, given as (Hildebrand et al. 2009):

$$\delta\theta \simeq \frac{\langle B_{\text{t}}^2 \rangle^{1/2}}{B} = \frac{b}{\sqrt{2 - b^2}}. \quad (8)$$

When $B_{\text{t}} \ll B$, i.e., $b \ll 1$ rad, we can obtain $\delta\theta \sim b/\sqrt{2}$. We calculated the $D_{\theta}^{1/2}(\ell)$ for G351 using equation 6 and fitted with the quadratic function given as equation 7. The structure function plot for G351 is shown in Figure 4b. We only fitted the data points between $\sim 18''2$ and $\sim 40''$, to avoid fitting large-scale structures. The lower fitting limit was set to the resolution of the polarization data, whereas the upper limit was chosen based on visual inspection of the structure function, corresponding to the scale just before it reached saturation. The best-fit parameters for G351 are $b = 11.8^\circ \pm 1.5^\circ$ and $m = 0.53^\circ \pm 0.01^\circ$. The polarization angle dispersion (δ_{θ}) for the G351 cloud is $8.3^\circ \pm 1.5^\circ$. We further note that the angular dispersion analysis adopted here does not explicitly account for the integration of polarized emission along the LOS and within the telescope beam. Houde et al. (2009) showed that such beam and volume integration effects systematically reduce the observed angular dispersion by averaging over multiple turbulent cells, which in turn leads to an overestimation of the B_{POS} if uncorrected. Incorporating this effect generally results in a lower effective angular dispersion and therefore a reduction of the inferred B_{POS} , in some cases by factors of a few, depending on the physical beam size and the turbulent correlation length.

We also utilized the sliding box method presented in Hwang

¹ <https://github.com/catherinezucker/radfil>

et al. (2021), to generate a pixel-by-pixel polarization angle dispersion map. We proceed by defining a box of 20×20 pixels (pixel scale $\sim 4''.55$), which is approximately 5 times the beam size of the SOFIA/HAWC+ band D observations ($\sim 18''.2$) centered on the i^{th} pixel (Guerra et al. 2021; Lê et al. 2024). We estimate the root-mean-squared (RMS) of all the pixel values inside the box. This RMS value corresponds to the polarization angle dispersion at i^{th} pixel. This process is repeated by sliding the box across the entire region to generate the polarization dispersion map. The dispersion value for a given box is computed only if more than 50% of the pixels within it have valid (non-NaN) values; otherwise, the central pixel is excluded from the calculation. The mean polarization angle dispersion values toward the G351 cloud is $12.5^\circ \pm 5.3^\circ$. The polarization dispersion values toward G351 using both methods are nearly identical and cannot be distinguished within the error bars.

3.4.3 Velocity dispersion

The $\text{C}^{18}\text{O}(2-1)$ molecular line data is employed to estimate ΔV_{nt} for the G351 cloud. We obtained σ_v using the $\text{C}^{18}\text{O}(2-1)$ moment-2 map. The FWHM of the velocity component is calculated as, $\Delta V = 2.355 \times \sigma_v$. However, this value also consists the contribution of the thermal component of the velocity. To obtain the non-thermal velocity component we use the equation (Fuller & Myers 1992; Kauffmann et al. 2013)

$$\Delta V_{\text{nt}}^2 = \Delta V^2 - 8 \ln 2 \frac{kT}{m_{\text{C}^{18}\text{O}}}, \quad (9)$$

where k is the Boltzmann constant, T is the gas temperature (20 K), and $m_{\text{C}^{18}\text{O}}$ is the mass of C^{18}O molecule which is 30 amu. Figure 3c shows the $\text{C}^{18}\text{O}(2-1)$ moment-2 map (ΔV) toward the G351 cloud. The mean ΔV_{nt} value toward G351 is $1.47 \pm 0.41 \text{ km s}^{-1}$.

3.4.4 Magnetic field strength and mass-to-flux ratio

To derive the B_{POS} map toward the G351 cloud, $n(\text{H}_2)$, $\delta\theta$, and ΔV maps to a common angular resolution ($\sim 32''$) and pixel scale ($\sim 14''.32$), same as the $\text{C}^{18}\text{O}(2-1)$ molecular line data. By substituting the $n(\text{H}_2)$, $\delta\theta$, and ΔV maps into equation 4, we derived the B_{POS} map toward the G351 cloud (Figure 5a). The B_{POS} values reach up to $\sim 0.8 \text{ mG}$ toward c1. The mean B_{POS} obtained from the map is $\sim 170 \pm 127 \mu\text{G}$ across the filament. Using the structure function (SF) method, we derived a mean B_{POS} of $\sim 147 \pm 60 \mu\text{G}$.

To infer the relative importance of B-fields with respect to gravity, we use a parameter known as the mass-to-flux ratio, λ , which is estimated using the relation given by (Crutcher 2004)

$$\lambda_{\text{obs}} = \frac{(M/\Phi)_{\text{observed}}}{(M/\Phi)_{\text{critical}}} = 7.6 \times 10^{-21} \frac{N(\text{H}_2)}{B_{\text{tot}}}, \quad (10)$$

where B_{tot} is the total B-field strength in μG which is given as, $B_{\text{tot}} = 1.3 \times B_{\text{POS}}$ (Crutcher 2004). If $\lambda > 1$ signifies the dominance of gravity over the B-field, hence referred to as magnetically supercritical. Conversely, if $\lambda < 1$, it denotes that the B-field is dominant over gravity, characterizing those areas as magnetically subcritical. The mass-to-flux ratio toward the G351 cloud is $\sim 0.9 \pm 0.6$, characterizing the cloud as magnetically transcritical. Although the cloud is magnetically transcritical, the mass-to-flux ratio map shows $\lambda > 1$ values near the c1, indicating a relative dominance of gravity over the B-field.

3.5 Energy Balance

Star formation activity in a cloud is driven by a complex interplay of gravity, turbulence, and B-fields. Therefore, quantifying the relative contributions of these forces is essential to understand their roles in the physical processes governing star formation. Below present the virial theorem including these energies.

$$\frac{1}{2}\ddot{I} = 2E_{\text{K}} + E_{\text{B}} + E_{\text{G}} \quad (11)$$

Assuming a cylindrical geometry for the filament, the gravitational energy is given by (Fiege & Pudritz 2000)

$$E_{\text{G}} = \frac{-GM^2}{L}, \quad (12)$$

where M is the mass of the filament ($\sim 4150 M_{\odot}$), and L is the length of the filament ($\sim 7.8 \text{ pc}$). The kinetic energy is given by (Fiege & Pudritz 2000)

$$E_{\text{K}} = M\sigma_v^2, \quad (13)$$

where σ_v is the total velocity dispersion. The magnetic energy is given by (Crutcher 2012)

$$E_{\text{B}} = \frac{B^2V}{8\pi}, \quad (14)$$

where B is the POS strength of B-field, V is the volume of the cylinder. The E_{G} , E_{K} , and E_{B} values for G351 are $1.88 \pm 1.88 \times 10^{47}$ ergs, $1.79 \pm 1.04 \times 10^{47}$ ergs, and $3.20 \pm 2.24 \times 10^{47}$ ergs, respectively. Taking into account the uncertainties in the mass estimates compared to the previous studies, discussed in Section 3.3.2, the derived gravitational, kinetic, and magnetic energies could be underestimated by up to factors of four, two, and two, respectively. Within the associated uncertainties, the results indicate that the B-field, gravity, and turbulence contribute comparably to the overall energy budget of the cloud.

4 DISCUSSION

The SOFIA/HAWC+ $214 \mu\text{m}$ polarization observations revealed hourglass-shaped POS B-field toward clump c1 in the G351 cloud (Section 3.2). This morphology can be interpreted in two ways: either as a consequence of gravitational contraction, or as the result of converging sub-filaments aligned with the B-field, channeling material into the dense central hub. Both scenarios emphasize the role of B-fields in regulating mass assembly. In the following sections (i.e., Section 4.1 and 4.2), we examine these two possibilities in detail.

4.1 Hourglass-shaped B-field due to magnetically regulated collapse

The POS B-field inferred from the Planck observations is predominantly perpendicular to the major axis of the G351 filament, consistent with previous dust polarization studies of filamentary clouds (e.g., Planck Collaboration et al. 2016; Soler & Hennebelle 2017). The high-resolution SOFIA/HAWC+ $214 \mu\text{m}$ observations reveal an hourglass morphology of the B-field toward the massive star cluster associated with c1/IRAS 17233-3606 (see Figure 2a). The B-field lines in the rest of the filament are perpendicular to the major axis of the filament, consistent with the Planck observations, except the northernmost and southernmost regions of the filament, where the

B-field orientations are aligned parallel to the spine of the filament. Using the DCF method, the B_{POS} toward the G351 cloud is estimated to be $\sim 147 \pm 60 \mu\text{G}$, while the B_{POS} map (see Figure 5a) reveals values up to 0.8 mG near c1. The B-field energy and strength estimates together indicate that the B-fields are dynamically important in the G351 cloud (see Section 3.5). Through numerical simulation, Nakamura & Li (2008) discussed the evolution of a magnetized filamentary cloud. In this scenario, the initial system is dominated by the B-field, followed by turbulence and gravity. The subsequent evolution depends on the relative contributions of turbulence and gravitational forces. As discussed in Nakamura & Li (2008), when turbulence is insufficient to counteract gravitational settling along the B-field lines (see also Mouschovias & Spitzer 1976), gravity begins to overcome the magnetic pressure in the cross-field direction, where the B-field provides the main support. Ambipolar diffusion within the dense condensations further weakens magnetic support, allowing these regions to become self-gravitating. As the dense clump undergoes gravitational collapse, it locally distorts and bends the B-field lines, producing a pinched, hourglass-like morphology. These condensations then continue to collapse to form stars, with their evolution still partially regulated by the surrounding B-field. This scenario is supported by the mass-to-flux ratio analysis of the G351 cloud (see Figure 5), which shows that the cloud is magnetically transcritical on large scales, but becomes magnetically critical ($\lambda > 1$) near c1. Since the clump is massive enough to overcome the magnetic support, it distorts the initially perpendicular B-field lines, resulting in an hourglass-shaped morphology. Furthermore, the B-fields provide additional support that suppresses the formation of low-mass stars, allowing material to accumulate and eventually favoring the formation of massive stars. This B-field morphology observed in the G351 cloud is also supported by results from other MHD simulations as well. Gómez et al. (2018) demonstrated that B-field lines initially oriented perpendicular to a filament can be bent by gas flows driven by self-gravity, giving rise to a characteristic ‘U’-shaped structure along the filament. In the case of c1, which is accreting material along the filament from both sides, these converging gas flows bend the field lines inward from both directions, resulting in an hourglass-shaped B-field morphology. A longitudinal velocity gradient along a filament is an observational signature of such mass accretion (Mallick et al. 2023). However, no such gradient is detected in the $\text{C}^{18}\text{O}(2-1)$ data for the G351 filament, likely due to the filament’s small projection along the line of sight.

Overall, the B-field plays a dominant role in regulating the dynamics of the G351 cloud, while gravitational forces locally distort the field lines, producing the observed hourglass-shaped magnetic morphology.

4.2 Hourglass-shaped B-field due to converging sub-filaments

Considering that the magnetic and gravitational energies in the G351 cloud are comparable, the observed hourglass B-field morphology may also be influenced by the converging sub-filaments. Leurini et al. (2019) reported multiple sub-filaments feeding into the central filamentary structure, consistent with accretion from the surrounding medium. In general, the B-field lines tends to align parallel to low-density filaments (or striations), while it becomes perpendicular to the higher-density filaments. This transition in field orientation typically occurs at column densities of about $N(\text{H}_2) \sim 5 \times 10^{21} \text{cm}^{-2}$. This behavior has been confirmed observationally and is also reproduced in MHD simulations (Soler et al. 2013; Planck Collaboration et al. 2015, 2016; Soler & Hennebelle 2017). Figure 6 shows the SOFIA/HAWC+ 214 μm B-field vectors overlaid on the *Spitzer*

8.0 μm image. A closer inspection shows that the B-field lines are aligned with the sub-filaments surrounding the central filament. While, the field lines are perpendicular to high density regions of filament. A similar signature is also observed in the Musca filament where the B-field lines are perpendicular to high-density filament, while parallel to the surrounding low-density striations (Cox et al. 2016). In this scenario, the alignment of the sub-filaments with the B-field suggests that material is being accreted preferentially along the field lines, indicating B-field channeled mass inflow toward the central filament. Because the sub-filaments in the G351 cloud are not perpendicular to the main filament, the B-field remains aligned with the low-density striations but turns perpendicular within the higher-density regions (see green arrows in Fig: 6). This transition in field orientation naturally give rise to an hourglass-shaped field morphology. A similar pattern is seen near the massive star-forming region around clump c1, where the ‘U’-shaped structure on either side of the clump shows a resemblance to an hourglass morphology. In this case, however, the apparent hourglass shape likely arises from the convergence of the sub-filaments rather than from a classical, gravitationally induced pinching of the B-field. Leurini et al. (2019) investigated the G351 filament using *Herschel* multi-wavelength data and identified several sub-filaments converging toward the central filament and clump c1. Such a configuration is characteristic of a hub-filament system (HFS), in which multiple low aspect-ratio filaments feed material into a dense central hub where massive stars form (Myers 2009). The B-field lines in this study are aligned with the sub-filaments surrounding the clump c1, which is active massive star-forming region in the G351 filament. A similar behaviour is also reported in Serpens South by Pillai et al. (2020), where the B-field lines are observed to follow the inflowing filaments and guide material toward the main hub.

Given the limitations of the current datasets, it is not possible to determine which physical process predominantly drives the hourglass-shaped B-field geometry toward c1. It remains plausible that both gravitational contraction and magnetically guided inflow along sub-filaments act together to produce the observed morphology. Hence, high-resolution polarimetric and spectral-line observations toward c1 are required to distinguish between these scenarios.

4.3 Comparison with other filamentary clouds and important caveats

The B-field morphology observed in the G351 filamentary cloud shows a striking resemblance to the B-field structure in the Orion A/OMC-1 filament (e.g., Pattle et al. 2017; Chuss et al. 2019; Hwang et al. 2021), as revealed by the JCMT and SOFIA observations. Previous studies of the OMC-1 filament have shown that the B-field lines are predominantly perpendicular to the filament, whereas toward the dense regions, the field exhibits an hourglass-like morphology. The mass-to-flux ratio and energy analyses indicate that the magnetic energy dominates the overall energy budget, followed by turbulence and gravity. However, within the dense regions, the relative importance of gravity increases (Pattle et al. 2017; Hwang et al. 2021). The overall characteristics of B-field in OMC-1 are remarkably similar to those observed in the G351 cloud in this study. A similar B-field configuration has been reported in the massive DR21 filament using JCMT/POL-2 and SCUBA-2 observations (Ching et al. 2022). In this filament, the B-field lines are predominantly perpendicular to the main pc-scale filament, while toward the massive dense core in the southern region, the field exhibits an hourglass-like morphology. Although similar B-field configurations have been observed in other filaments such as OMC-1 and DR21,

reports of pinched, hourglass-shaped B-fields in IRDCs are limited, highlighting the critical role of B-fields in regulating the physical processes in the early stages of star formation.

The B_{POS} and λ values estimated using the DCF method carry significant uncertainties, potentially up to a factor of two or more. The main contribution comes from the value of correction factor Q in equation 4. Numerous 3D MHD simulations have shown that this correction factor can vary from 0.2–1 depending on the turbulence regime, cloud geometry, and projection angle (Liu et al. 2021; Chen et al. 2022; Myers et al. 2024). In particular, studies indicate that in strongly magnetized systems, the basic assumptions of the DCF method—namely small angular perturbations and approximate equipartition between turbulent kinetic and magnetic energy are better satisfied, and the correction factor approaches unity. In contrast, in weakly magnetized or self-gravitating systems, departures from equipartition, enhanced line-of-sight averaging, and unresolved field curvature lead to systematically smaller correction factors, typically $Q \sim 0.3$ –0.4. Additionally, assumptions such as the cylindrical geometry of the filament cannot be precisely quantified and may contribute further to the uncertainties in the estimated B_{POS} values. The kinetic or turbulent energy can arise from two main sources: the cloud’s intrinsic turbulence and the turbulence injected by stellar feedback. Consequently, it is difficult to disentangle the contributions of these two factors. Additionally, projection effects, including the unknown filament inclination and line-of-sight averaging, can bias the POS B-field strength measurements. In cases where the B-field strength is overestimated, the filament would transition from a magnetically transcritical state to a marginally supercritical regime. We therefore emphasize that the DCF-based estimates presented here should be interpreted as order-of-magnitude constraints, and that G351 lies close to the critical mass-to-flux threshold within the combined observational and methodological uncertainties.

5 SUMMARY AND CONCLUSION

We present a multi-wavelength study of the G351 IRDC, including the SOFIA/HAWC+ polarimetric observations at 214 μm . The key findings of this study are summarized as follows:

(i) A total of 53 Class I YSOs are identified toward the G351 cloud using the [4.5]–[5.8] vs [3.6]–[4.5] CCD. Most of these YSOs are located along the filamentary cloud, confirming active star formation within the region.

(ii) The POS B-field morphology inferred from the SOFIA/HAWC+ 214 μm polarization data reveal that the B-field orientations are predominantly perpendicular to the major axis of the G351 filament.

(iii) The B-field strength toward the G351 filament, estimated using the DCF method, is $\sim 147 \pm 60 \mu\text{G}$. The mass-to-flux ratio analyses indicate that the filament is in a magnetically transcritical state ($\lambda \sim 1$), where the gravitational and magnetic energies are comparable.

(iv) The energy budget analysis reveals that the magnetic, kinetic, and gravitational energies contribute comparably in the G351 cloud,

(v) The POS B-field orientations toward the clump c1 reveals an hourglass-shaped morphology, with the B-field strengths values

reaching upto ~ 0.8 mG.

(vi) The hourglass-shaped B-field toward c1 may arise from magnetically regulated gravitational collapse, from magnetically aligned converging sub-filaments, or from a combination of both processes.

Overall, our results show that the B-fields are dynamically important in regulating the massive star formation activity in the G351 filamentary cloud.

ACKNOWLEDGMENTS

The research work at Physical Research Laboratory is funded by the Department of Space, Government of India. IIZ is supported by the IAP RAS project FFUF-2024-0028. This publication is based on data acquired with the Atacama Pathfinder Experiment (APEX) under the programme ID 0104.F-9301(A). APEX is a collaboration between the Max-Planck-Institut für Radioastronomie, the European Southern Observatory, and the Onsala Space Observatory. PS was partially supported by a Grant-in-Aid for Scientific Research (KAKENHI Number JP23H01221) of JSPS. RKY gratefully acknowledges support from the Fundamental Fund of Thailand Science Research and Innovation (TSRI) through the National Astronomical Research Institute of Thailand (Public Organization) (FFB680072/0269). This research has made use of the NASA/IPAC Infrared Science Archive, which is funded by the National Aeronautics and Space Administration and operated by the California Institute of Technology. The MeerKAT telescope is operated by the South African Radio Astronomy Observatory, which is a facility of the National Research Foundation, an agency of the Department of Science and Innovation.

Data availability

The *Herschel*, *Spitzer* and SOFIA data underlying this article are available from the publicly accessible NASA/IPAC infrared science archive². The unWISE data underlying this article are available from the publicly accessible website³. The *Herschel* column density and temperature maps underlying this article are available from the publicly accessible website⁴. The SARAO MeerKAT 1.3 GHz continuum data underlying this article are available from the publicly accessible server⁵. The ATLASGAL 870 μm dust continuum clumps underlying this article are available from the publicly accessible VizieR archive for catalogues⁶.

REFERENCES

- Añez-López N., et al., 2020, *A&A*, **644**, A52
 André P., Di Francesco J., Ward-Thompson D., Inutsuka S. I., Pudritz R. E., Pineda J. E., 2014, in Beuther H., Klessen R. S., Dullemond C. P., Henning T., eds, *Protostars and Planets VI*. pp 27–51 ([arXiv:1312.6232](https://arxiv.org/abs/1312.6232)), [doi:10.2458/azu_uapress_9780816531240-ch002](https://doi.org/10.2458/azu_uapress_9780816531240-ch002)
 Arzoumanian D., et al., 2011, *A&A*, **529**, L6

² <https://irsa.ipac.caltech.edu/frontpage/>

³ <https://unwise.me/>

⁴ <http://www.astro.cardiff.ac.uk/research/ViaLactea/>

⁵ <https://archive-gw-1.kat.ac.za/public/repository/10.48479/3wfd-e270/index.html>

⁶ <https://cdsarc.cds.unistra.fr/viz-bin/cat/>

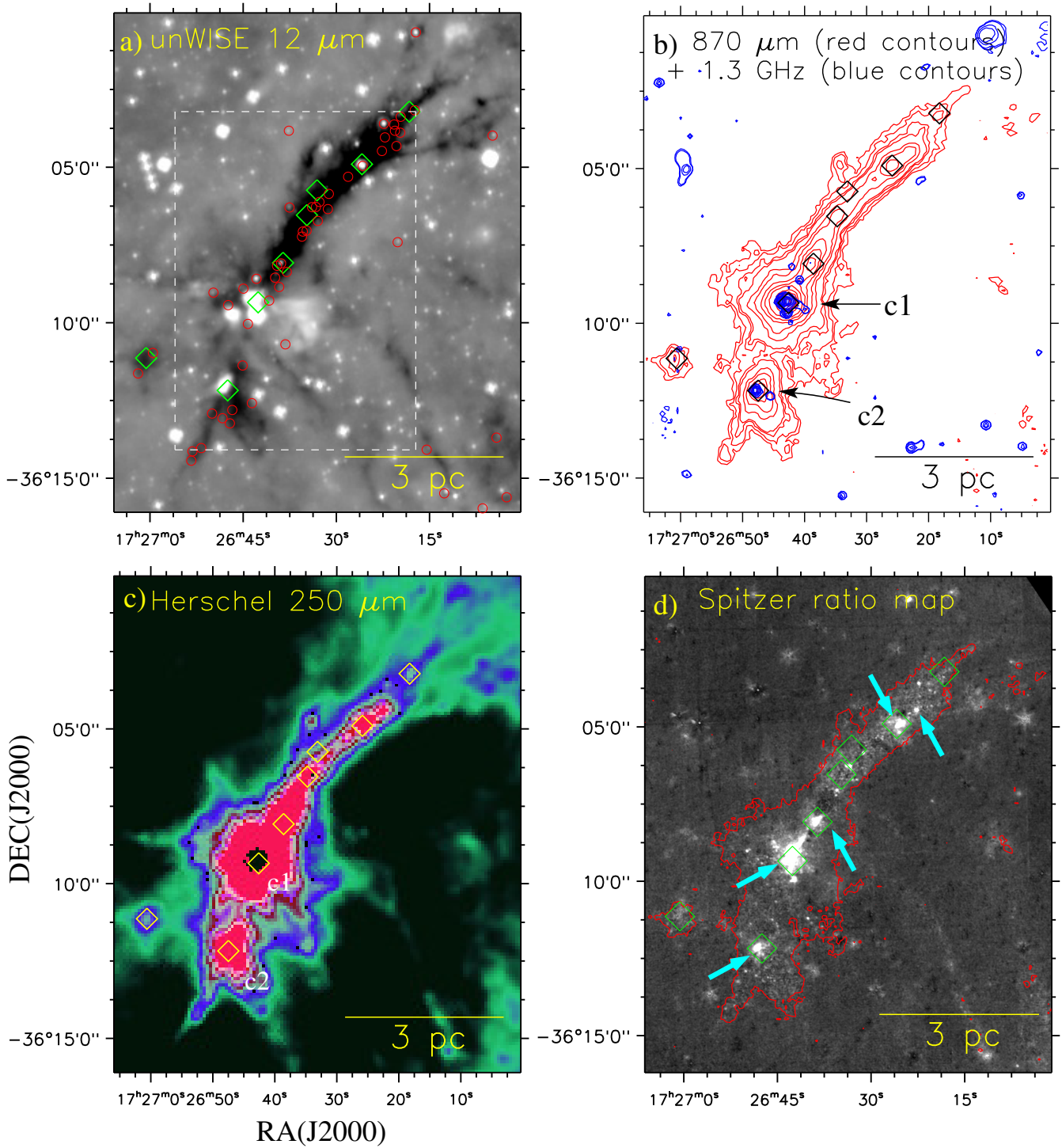


Figure 1. a) unWISE 12.0 μm image of the G351 cloud overlaid with the positions of YSOs (red circles) identified using $[5.8]-[4.5]$ vs $[3.6]-[4.5]$ CCD (see text for more details). The white dashed box highlights the area shown in Figure 3a–3d. b) An overlay of SMGPS 1.3 GHz continuum emission contours (in blue) on ATLASGAL 870 μm contours (in red). The red contour levels are 0.14, 0.24, 0.38, 0.48, 0.94, 1.41, 2.35, 3.30, 4.71, 9.42, 14.12, 18.83, 23.54, 37.66, and 42.37 mJy beam^{-1} . The blue contour levels are 0.44, 0.88, 2.6, 4.4, 6.2, 8.8, 18, 26, 35, 44, 70, and 79 mJy beam^{-1} . c) *Herschel* 250 μm image of the G351 cloud. d) *Spitzer* 4.5 $\mu\text{m}/3.6 \mu\text{m}$ ratio map of the G351 cloud overlaid with the 870 μm emission contour level at 0.14 mJy beam^{-1} . The cyan arrows are used to highlight the bright regions where star formation activity is prominent. The diamonds show the positions of ATLASGAL clumps. The scale bar corresponds to 3 pc at a distance of 2.0 kpc.

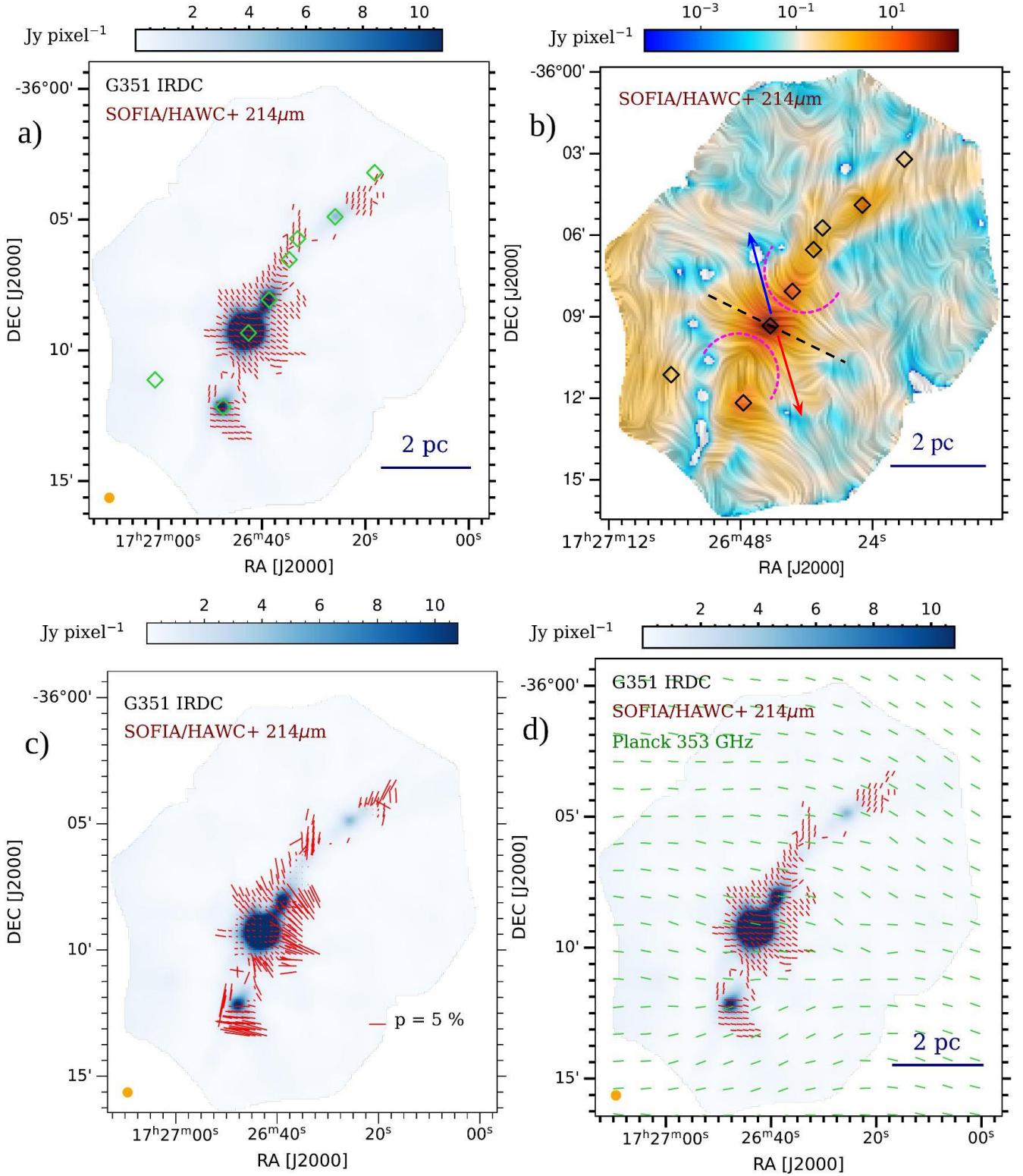


Figure 2. a) SOFIA/HAWC+ 214 μm image of the G351 overlaid with the red segments showing the direction of the B-field derived using the SOFIA/HAWC+ 214 μm polarization observations. b) The LIC map showing the B-field same as Figure 2a, overlaid on the SOFIA/HAWC+ 214 μm intensity map. The magenta curves highlight the hourglass-shaped B-field. The red and blue arrows show the direction of outflow toward IRAS 17233–3606. The black dashed line shows the direction of velocity gradient (Klaassen et al. 2015). c) Same as Figure 2a, with length of the segments proportional to the polarization fraction. A reference segment corresponding to a 5% polarization fraction is shown in the bottom-right corner of the panel. d) Same as Figure 2a, overlaid with B-field segments (in green) inferred using the Planck 353 GHz data. The diamonds show the positions of ATLASGAL clumps. The beam size of the SOFIA/HAWC+ 214 μm observations ($\sim 18''$) is indicated by a filled orange circle. The scale bar corresponds to 2 pc at a distance of 2.0 kpc.

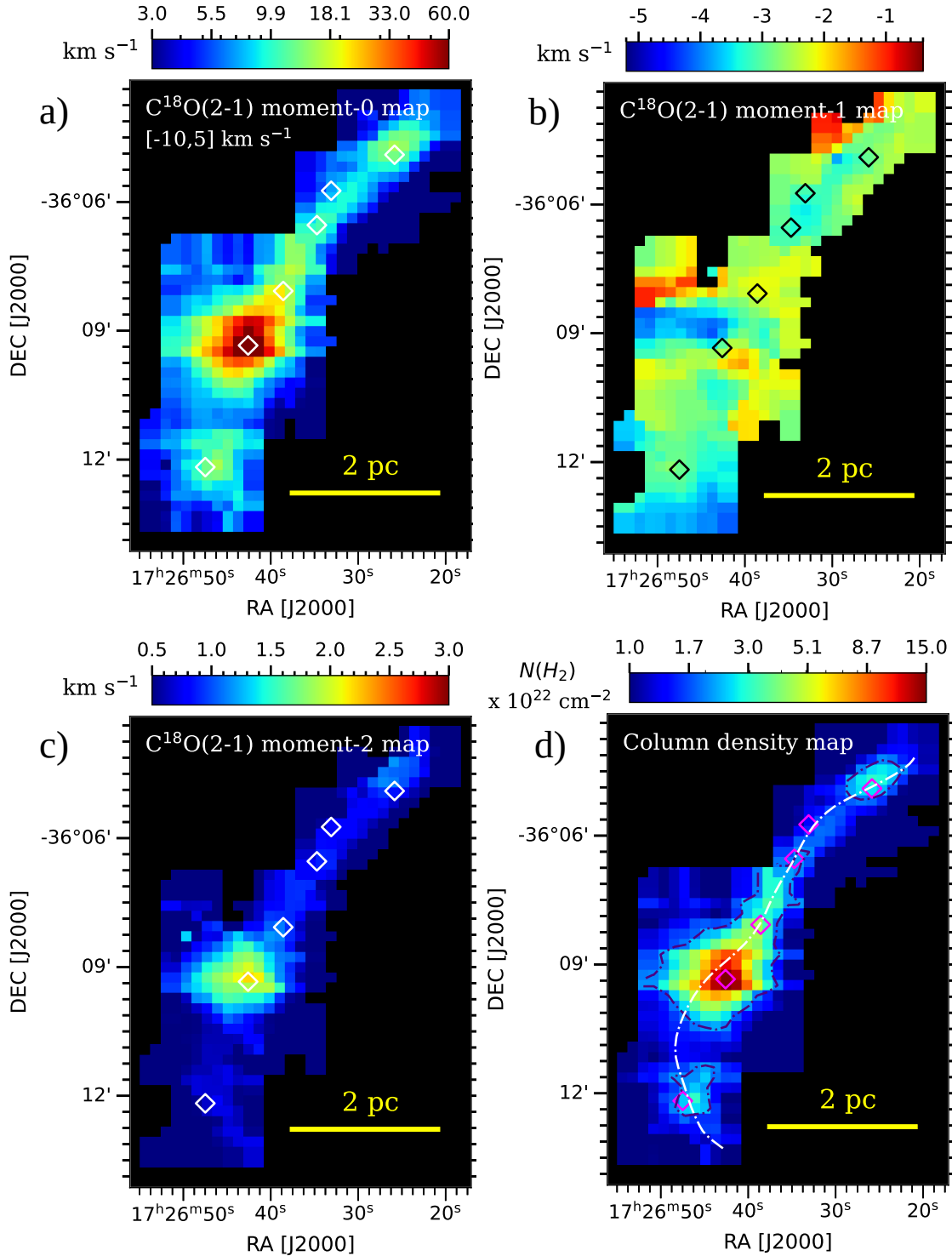


Figure 3. a) C¹⁸O(2–1) moment-0 map of the G351 cloud integrated over a range of $[-10, 5] \text{ km s}^{-1}$. b) C¹⁸O(2–1) moment-1 map. c) C¹⁸O(2–1) moment-2 map. d) $N(H_2)$ map of the G351 cloud. The contour level is $1.6 \times 10^{22} \text{ cm}^{-2}$. The dot-dashed line shows the spine of the filament identified using the RadFil algorithm. The scale bar and symbols are same as Figure 2.

Benjamin R. A., et al., 2003, *Publications of the Astronomical Society of the Pacific*, 115, 953

Beuther H., Ahmadi A., Mottram J., Bosco F., Linz H., Klaassen P., CORE Team 2017, *Mem. Soc. Astron. Italiana*, 88, 584

Beuther H., et al., 2019, *A&A*, 621, A122

Beuther H., Olguin F. A., Sanhueza P., Cunningham N., Ginsburg A., 2025,

A&A, 695, A51

Chambers E. T., Jackson J. M., Rathborne J. M., Simon R., 2009, *ApJS*, 181, 360

Chandrasekhar S., Fermi E., 1953, *ApJ*, 118, 113

Chen C.-Y., Ostriker E. C., 2015, *ApJ*, 810, 126

Chen C.-Y., Li Z.-Y., Mazzei R. R., Park J., Fissel L. M., Chen M. C.-Y.,

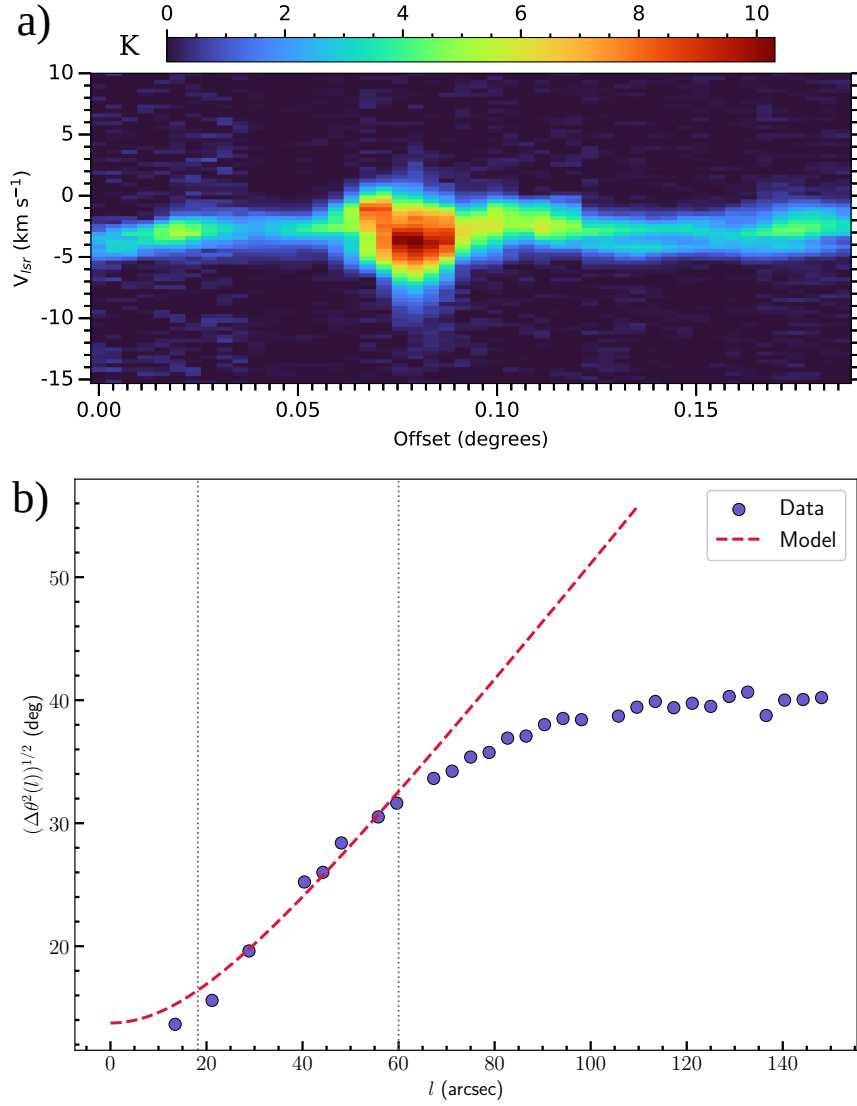


Figure 4. a) PV diagram along the spine of the filamentary cloud shown in Figure 3d. b) The panel presents the structure function ($D_{\theta}^{1/2}(\ell)$) for the G351 cloud. The red dashed line shows the linear fit of Equation 7, while the gray vertical dashed lines mark the lower and upper limits used for the fit.

Klein R. I., Li P. S., 2022, *MNRAS*, 514, 1575
 Chen Z., Sefako R., Yang Y., Jiang Z., Su Y., Zhang S., Zhou X., 2023, *MNRAS*, 525, 107
 Ching T.-C., et al., 2022, *ApJ*, 941, 122
 Chuss D. T., et al., 2019, *ApJ*, 872, 187
 Coudé S., et al., 2025, *arXiv e-prints*, p. arXiv:2509.25832
 Cox N. L. J., et al., 2016, *A&A*, 590, A110
 Crutcher R. M., 2004, *Ap&SS*, 292, 225
 Crutcher R. M., 2012, *ARA&A*, 50, 29
 Dewangan L. K., Luna A., Ojha D. K., Anandarao B. G., Mallick K. K., Mayya Y. D., 2015, *ApJ*, 811, 79
 Fiege J. D., Pudritz R. E., 2000, *ApJ*, 544, 830
 Fuller G. A., Myers P. C., 1992, *ApJ*, 384, 523
 Getman K. V., Feigelson E. D., Garmire G., Broos P., Wang J., 2007, *ApJ*, 654, 316
 Ginsburg A., et al., 2023, *ApJ*, 942, 66
 Goedhart S., et al., 2024, *MNRAS*, 531, 649
 Gómez G. C., Vázquez-Semadeni E., Zamora-Avilés M., 2018, *MNRAS*, 480, 2939
 Guerra J. A., Chuss D. T., Dowell C. D., Houde M., Michail J. M., Siah J.,

Wollack E. J., 2021, *ApJ*, 908, 98
 Harper D. A., et al., 2018, *Journal of Astronomical Instrumentation*, 07, 1840008
 Hartmann L., Megeath S. T., Allen L., Luhman K., Calvet N., D'Alessio P., Franco-Hernandez R., Fazio G., 2005, *ApJ*, 629, 881
 Hildebrand R. H., Kirby L., Dotson J. L., Houde M., Vaillancourt J. E., 2009, *ApJ*, 696, 567
 Houde M., Dowell C. D., Hildebrand R. H., Dotson J. L., Vaillancourt J. E., Phillips T. G., Peng R., Bastien P., 2004, *ApJ*, 604, 717
 Houde M., Vaillancourt J. E., Hildebrand R. H., Chitsazzadeh S., Kirby L., 2009, *ApJ*, 706, 1504
 Hwang J., et al., 2021, *ApJ*, 913, 85
 Hwang J., et al., 2025, *ApJ*, 985, 222
 Ishihara K., et al., 2024, *ApJ*, 974, 95
 Jadhav O. R., et al., 2025, *ApJ*, 986, 48
 Kauffmann J., Pillai T., Goldsmith P. F., 2013, *ApJ*, 779, 185
 Klaassen P. D., Johnston K. G., Leurini S., Zapata L. A., 2015, *A&A*, 575, A54
 Lamarre J. M., et al., 2010, *A&A*, 520, A9
 Lang D., 2014, *AJ*, 147, 108

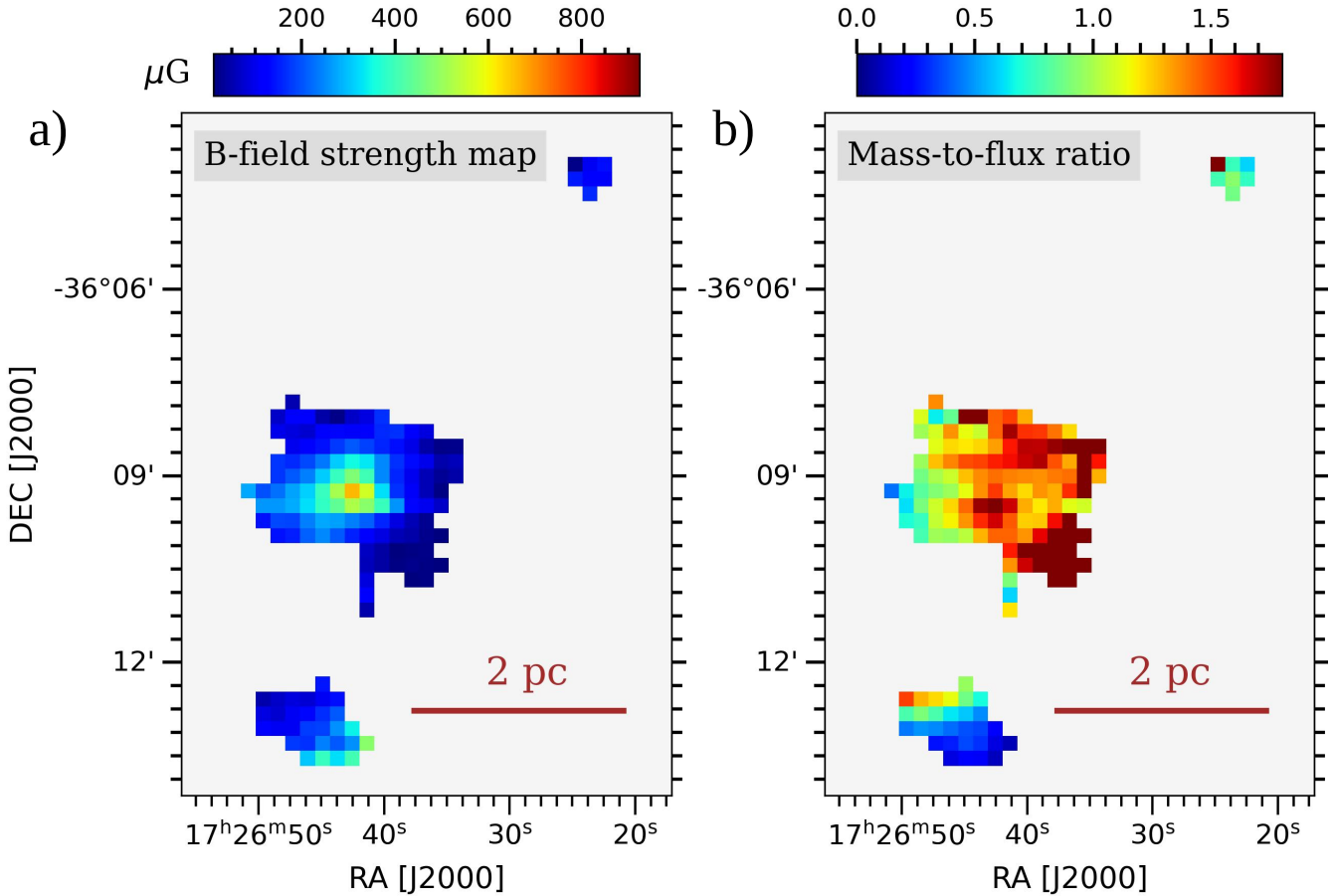


Figure 5. a) B-field strength map of the G351 cloud. b) Mass-to-flux ratio map of the G351 cloud. The scalebar in each panel is same as Figure 2.

- Law C.-Y., et al., 2024, *ApJ*, 967, 157
Lê N., et al., 2024, *A&A*, 690, A191
Leurini S., Hieret C., Thorwirth S., Wyrowski F., Schilke P., Menten K. M., Güsten R., Zapata L., 2008, *A&A*, 485, 167
Leurini S., et al., 2009, *A&A*, 507, 1443
Leurini S., Codella C., Zapata L., Beltrán M. T., Schilke P., Cesaroni R., 2011a, *A&A*, 530, A12
Leurini S., Pillai T., Stanke T., Wyrowski F., Testi L., Schuller F., Menten K. M., Thorwirth S., 2011b, *A&A*, 533, A85
Leurini S., Codella C., Gusdorf A., Zapata L., Gómez-Ruiz A., Testi L., Pillai T., 2013, *A&A*, 554, A35
Leurini S., et al., 2019, *A&A*, 621, A130
Li P. S., Lopez-Rodriguez E., Soam A., Klein R. I., 2022, *MNRAS*, 514, 3024
Lietzow-Sinjen M., Wolf S., Brunngräber R., 2025, *A&A*, 694, A190
Liu T., Wu Y., Zhang H., 2013, *ApJ*, 775, L2
Liu J., Zhang Q., Commerçon B., Valdivia V., Maury A., Qiu K., 2021, *ApJ*, 919, 79
Liu J., et al., 2024, *ApJ*, 966, 120
Maity A. K., et al., 2024, *ApJ*, 974, 229
Mallick K. K., Dewangan L. K., Ojha D. K., Baug T., Zinchenko I. I., 2023, *ApJ*, 944, 228
Mangum J. G., Shirley Y. L., 2015, *PASP*, 127, 266
Motte F., et al., 2022, *A&A*, 662, A8
Mouschovias T. C., Spitzer Jr. L., 1976, *ApJ*, 210, 326
Myers P. C., 2009, *ApJ*, 700, 1609
Myers P. C., Stephens I. W., Coudé S., 2024, *ApJ*, 962, 64
Nakamura F., Li Z.-Y., 2008, *ApJ*, 687, 354
Ngoc N. B., et al., 2023, *ApJ*, 953, 66
Norris R. P., Whiteoak J. B., Caswell J. L., Wieringa M. H., Gough R. G., 1993, *ApJ*, 412, 222
Pattle K., et al., 2017, *ApJ*, 846, 122
Pickett H. M., Poynter R. L., Cohen E. A., Delitsky M. L., Pearson J. C., Müller H. S. P., 1998, *J. Quant. Spectrosc. Radiative Transfer*, 60, 883
Pillai T., Kauffmann J., Tan J. C., Goldsmith P. F., Carey S. J., Menten K. M., 2015, *ApJ*, 799, 74
Pillai T. G. S., et al., 2020, *Nature Astronomy*, 4, 1195
Planck Collaboration et al., 2015, *A&A*, 576, A104
Planck Collaboration et al., 2016, *A&A*, 586, A138
Pravash S., Soam A., Diep P. N., Hoang T., Ngoc N. B., Tram L. N., 2025, *ApJ*, 981, 128
Rathborne J. M., Jackson J. M., Simon R., 2006, *ApJ*, 641, 389
Reyes-Reyes S. D., Stutz A. M., Megeath S. T., Xu F., Álvarez-Gutiérrez R. H., Sandoval-Garrido N., Liu H.-L., 2024, *MNRAS*, 529, 2220
Ryabukhina O. L., Zinchenko I. I., 2021, *MNRAS*, 505, 726
Sandoval-Garrido N. A., et al., 2025, *A&A*, 696, A202
Sanhueza P., Jackson J. M., Foster J. B., Garay G., Silva A., Finn S. C., 2012, *ApJ*, 756, 60
Sanhueza P., et al., 2025, *ApJ*, 980, 87
Santos F. P., Busquet G., Franco G. A. P., Girart J. M., Zhang Q., 2016, *ApJ*, 832, 186
Schleuning D. A., 1998, *ApJ*, 493, 811
Schuller, F. et al., 2009, *Astronomy and Astrophysics Journal*, 504, 415
Seifried D., Walch S., 2015, *MNRAS*, 452, 2410
Simon R., Rathborne J. M., Shah R. Y., Jackson J. M., Chambers E. T., 2006, *ApJ*, 653, 1325

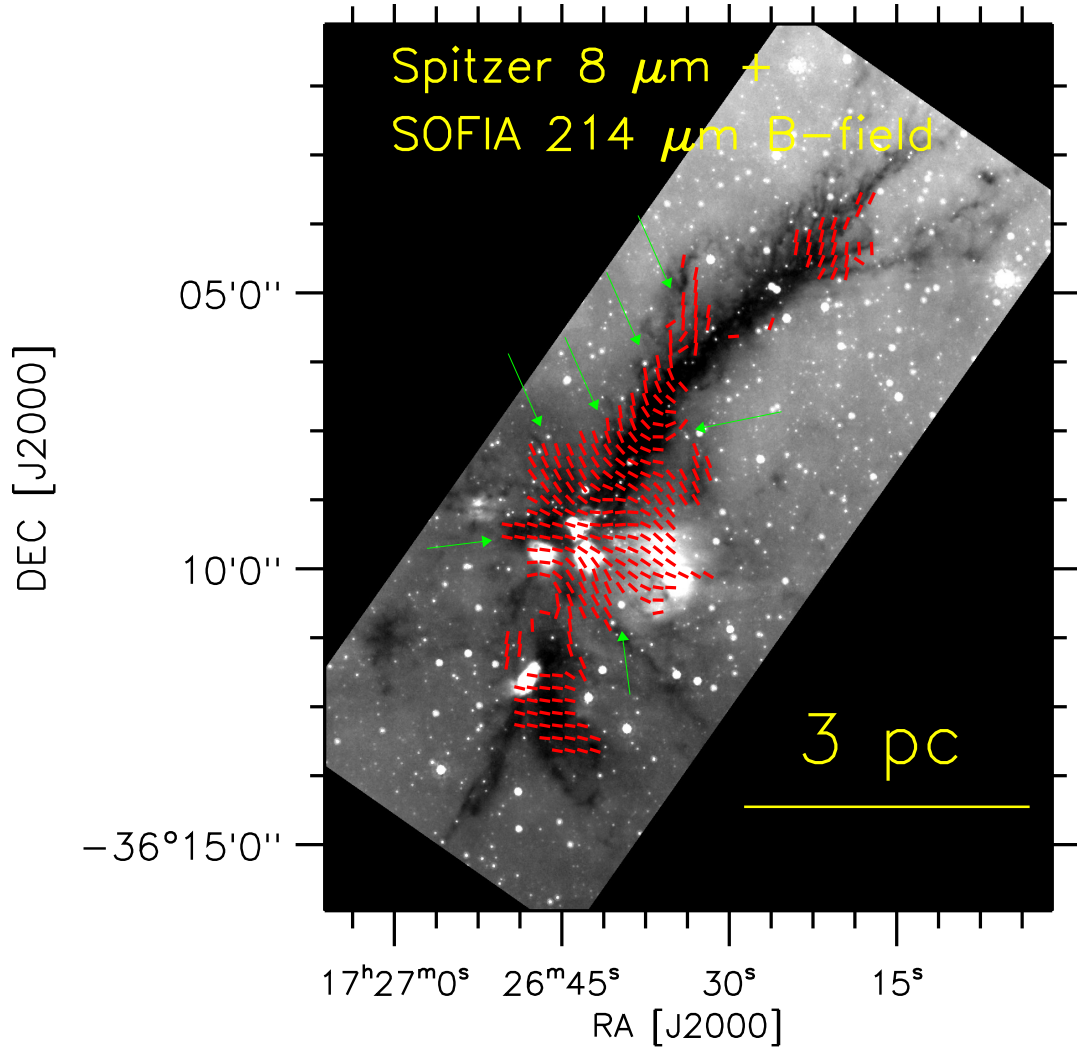


Figure 6. *Spitzer* 8.0 μm image overlaid with the segments derived from the SOFIA/HAWC+ 214 μm polarization data. The green arrows highlight the sub-filaments aligned with the local B-field orientations. The scale bar corresponds to 3 pc at a distance of 2.0 kpc.

- Soam A., et al., 2019, *ApJ*, 883, 95
 Soler J. D., Hennebelle P., 2017, *A&A*, 607, A2
 Soler J. D., Hennebelle P., Martin P. G., Miville-Deschênes M.-A., Netterfield C. B., Fissel L. M., 2013, *ApJ*, 774, 128
 Stephens I. W., et al., 2022, *ApJ*, 926, L6
 Stephens I. W., et al., 2025, *arXiv e-prints*, p. arXiv:2510.05933
 Tang Y.-W., Koch P. M., Peretto N., Novak G., Duarte-Cabral A., Chapman N. L., Hsieh P.-Y., Yen H.-W., 2019, *ApJ*, 878, 10
 Tram L. N., et al., 2023, *ApJ*, 946, 8
 Truong B., Hoang T., Bich Ngoc N., Chau Giang N., Tram L. N., Le N., 2025, *arXiv e-prints*, p. arXiv:2510.06726
 Urquhart J. S., et al., 2017, *Monthly Notices of the Royal Astronomical Society*, 473, 1059
 Walsh A. J., Burton M. G., Hyland A. R., Robinson G., 1998, *MNRAS*, 301, 640
 Yuan J., et al., 2016, *ApJ*, 820, 37
 Zapata L. A., Leurini S., Menten K. M., Schilke P., Rolfs R., Hieret C., 2008, *AJ*, 136, 1455
 Zielinski N., Wolf S., 2022, *A&A*, 659, A22
 Zucker C., Chen H. H.-H., 2018, *ApJ*, 864, 152